Published in final edited form as:
Cell. 2014 March 13; 156(6): 1193–1206. doi:10.1016/j.cell.2014.02.008.

Unified Polymerization Mechanism for the Assembly of ASC-dependent Inflammasomes

Alvin Lu[1,2,†], **VenkatGiri Magupalli**[1,2,†], **Jianbin Ruan**[1,2,†], **Qian Yin**[1,2], **Maninjay K. Atianand**[3], **Matthijn Vos**[4], **Gunnar F. Schröder**[5], **Katherine A. Fitzgerald**[3], **Hao Wu**[1,2,*], and **Edward H. Egelman**[6]

[1]Department of Biological Chemistry and Molecular Pharmacology, Harvard Medical School, Boston, MA 02115 [2]Program in Cellular and Molecular Medicine, Boston Children's Hospital, Boston, MA 02115 [3]Division of Infectious Diseases and Immunology, Department of Medicine, University of Massachusetts Medical School, Worcester, MA 01655 [4]FEI NanoPort, 5651 Eindhoven, Netherlands [5]Institute of Complex Systems, ForschungszentrumJülich, 52425 Jülich, Germany [6]Department of Biochemistry and Molecular Genetics, University of Virginia, Charlottesville, VA 22908

SUMMARY

Inflammasomes elicit host defense inside cells by activating caspase-1 for cytokine maturation and cell death. AIM2 and NLRP3 are representative sensor proteins in two major families of inflammasomes. The adaptor protein ASC bridges the sensor proteins and caspase-1 to form ternary inflammasome complexes, achieved through pyrindomain (PYD) interactions between sensors and ASC, and caspase activation and recruitment domain (CARD) interactions between ASC and caspase-1. We found that PYD and CARD both form filaments. Activated AIM2 and NLRP3 nucleate PYD filaments of ASC, which in turn cluster the CARD of ASC. ASC thus nucleates CARD filaments of caspase-1 leading to proximity-induced activation. Endogenous NLRP3 inflammasome is also filamentous. The cryo-EM structure of ASC^{PYD} filament at near-atomic resolution provides a template for homo- and hetero-PYD/PYD associations, as confirmed by structure-guided mutagenesis. We propose that ASC-dependent inflammasomes in both families share a unified assembly mechanism that involves two successive steps of nucleation-induced polymerization.

*Correspondence to: Hao Wu, Ph.D., Department of Biological Chemistry and Molecular Pharmacology, Harvard Medical School, Program in Cellular and Molecular Medicine, Boston Children's Hospital, 3 Blackfan Circle, Room 3099, Boston, MA 02115, Office: 617-713-8160, Fax: 617-713-8161, Admin: 617-713-8162, hao.wu@childrens.harvard.edu.
†These authors contributed equally.

ACCESSION NUMBERS

The cryo-EMmap of ASC^{PYD} filament was deposited to EMDataBank under accession code EMD-5830. The corresponding refined structure of ASC^{PYD} in the filament was deposited in the Protein Data Bank with ID code 3J63.

INTRODUCTION

The immune system provides protection from the environment and is critically important for multiple aspects of mammalian biology. It consists of an adaptive component that generates specific antibodies and cells through clonal selection, and an innate component that utilizes preformed receptors. Innate immunity offers the first line of defense against infections and hazards by directly recognizing conserved pathogen- and danger-associated molecular patterns (PAMPs and DAMPs) to alert the immune system (Medzhitov and Janeway, 2000). Inflammasomes are key components of innate immunity inside the cell. They are formed in response to PAMPs and DAMPs, and activate inflammatory caspases such as caspase-1 and -11 (Franchi et al., 2012; Lamkanfi and Dixit, 2012; Rathinam et al., 2012). Caspase activation can lead to proteolytic maturation of cytokines IL-1β and IL-18, and elicit the inflammatory form of cell death pyroptosis, as ways to control exogenous and endogenous invasions.

Inflammasomes are supramolecular assemblies composed of at least a sensor protein and a caspase, and often the adapter protein ASC. Based on the domain architecture of the sensor protein, inflammasomes maybe divided into two families. The first family is known as ALR [Absent in Melanoma 2 (AIM2)-like receptor], named after the first identified member (Figure 1A). ALRs are composed of an N-terminal PYD and one or two HIN domains (Rathinam et al., 2012). AIM2 directly senses the cytosolic PAMPs dsDNAs, such as those associated with viruses, using its HIN domain (Jin et al., 2012; Rathinam et al., 2012). The second class of inflammasomes contains receptors in the NLR [nucleotide-binding domain (NBD) and leucine rich repeat (LRR) – containing receptors] family (Figure 1A). NBD belongs to the AAA+ superfamily of ATPase domains. Most NLRs contain an N-terminal PYD and are known as NLRPs. The best-studied NLRP3 inflammasome is activated following a wide range of pathogen and danger signals including extra cellular ATP and uric acid crystals (Franchi et al., 2012; Lamkanfi and Dixit, 2012; Rathinam et al., 2012). Upon activation, both AIM2 and NLRP3 recruit the PYD- and CARD-containing bipartite adapter ASC (apoptosis-associated speck-like protein containing a CARD) through PYD/PYD interactions (Masumoto et al., 1999).ASC in turn recruits caspase-1 through CARD/CARD interactions (Figure 1A). PYD and CARD both belong to the death domain (DD) fold superfamily (Ferrao and Wu, 2012), for which structures of two defined DD helical assemblies are known (Lin et al., 2010; Park et al., 2007).

Malfunctioning of inflammasomes is associated with serious human diseases (Strowig et al., 2012). Mutations in inflammasome proteins NLRP3, NLRP12 and MEFV (also known as Pyrin) are linked to auto inflammatory and fever syndromes (Rathinam et al., 2012). Aberrations in NLR inflammasome activation have been connected to psoriasis, type II diabetes, inflammatory bowel diseases and Alzheimer’s disease (Franchi et al., 2012; Lamkanfi and Dixit, 2012; Rathinam et al., 2012; Strowig et al., 2012).The PYD-less ALR member, mouse p202, interacts with the HIN domain of AIM2 to inhibit inflammasome and potentiatelupus (Yin et al., 2013).

Immunofluorescence microscopy showed that transfected full-length ASC (ASC^{FL}) and endogenous ASC upon stimulation both form speck-like aggregates (Masumoto et al.,

1999). Because transfected PYD and CARD-only ASC fragments are filamentous (Masumoto et al., 2001), the specks are most likely dense, cross linked composites of PYD and CARD filaments. Because of the strong tendency of ASC to aggregate, the structures of ASC PYD (ASC^{PYD}) and ASC^{FL} were solved in monomeric states using nuclear magnetic resonance (NMR) at acidic conditions (de Alba, 2009; Liepinsh et al., 2003). Although additional monomeric PYD structures have been reported, including those of NLRP3 (Bae and Park, 2011) and AIM2 (Jin et al., 2013), the mode of homo- and hetero-PYD associations is entirely unknown.

Here, we used *in vitro* reconstitution, electron microscopy (EM) and polymerization assays to address assembly mechanisms for ASC-dependent AIM2 and NLRP3 inflammasomes. In contrast to the presumption that the different domain structures of AIM2 and NLRP3may lead to considerable differences in the inflammasome architectures, we showed that both AIM2 upon dsDNA interaction and NLRP3 oligomerized through its NBD nucleate ASC^{PYD} filaments. This is particularly surprising for NLRP3; due to the domain similarity of NLRs to Apaf-1-like molecules that form ring-like platforms (Yuan and Akey, 2013), the overarching paradigm had presumed that NLR inflammasomes are also ring-like structures. The flexibly linked ASC CARD (ASC^{CARD}) then clusters along the ASC^{PYD} filament to act as the platform for caspase-1^{CARD} filament formation, leading to proximity-induced caspase dimerization and activation. The ternary inflammasome complex showed star-shaped branched filamentous morphology, and exhibited unequal stoichiometries among the component proteins. We determined the cryo-EM structure of the ASC^{PYD} filament at near atomic resolution through helical reconstruction. The structure revealed molecular details of ASC^{PYD}/ASC^{PYD} interactions and allowed modeling of $AIM2^{PYD}$/ASC^{PYD} and $NLRP3^{PYD}$/ASC^{PYD} interactions. Structure-based mutagenesis confirmed the importance of ASC^{PYD}/ASC^{PYD}, $AIM2^{PYD}$/ASC^{PYD} and $NLRP3^{PYD}$/ASC^{PYD} interactions *in vitro* and in cells. EM of immuno precipitated endogenous NLRP3 inflammasome showed similar filamentous morphology as *in vitro* reconstituted inflammasomes and quantitative Western blotting confirmed the over-stoichiometry of caspase-1 to ASC. Our studies collectively revealed a universal assembly process for ASC-dependent inflammasomes in both ALR and NLR families that involves nucleation-induced polymerization.

RESULTS

The $AIM2^{PYD}$/ASC^{PYD} Complex is Filamentous with End Location of $AIM2^{PYD}$

To elucidate the assembly mechanisms for ASC-containing inflammasomes, we first reconstituted the interaction between AIM2 and ASC. Co-expression of $AIM2^{PYD}$ with ASC^{PYD} showed that the complex eluted at the void position of a Superdex 200 gel filtration column (Figure S1A), suggesting formation of large “aggregates”. We used EM to visualize the negatively stained $AIM2^{PYD}$/ASC^{PYD} complex, which revealed filaments with uniform diameters of ~9 nm (Figure 1B).

$AIM2^{PYD}$ exists in sub-stoichiometric molar ratio in the $AIM2^{PYD}$/ASC^{PYD} complex (Figure S1A, 1C). To understand this observation, we generated a construct of $AIM2^{PYD}$ capable of enzymatic biotinylation during expression. Co-expression of the $AIM2^{PYD}$ construct with ASC^{PYD} generated a complex with specific biotinylation of $AIM2^{PYD}$,

shown by streptavidin Western blotting (Figure 1C). Labeling biotinylated$AIM2^{PYD}$ by 6 nm streptavidin-gold particles showed that $AIM2^{PYD}$ is localized at one end of the filaments (Figure 1D). The number of bound gold particles varies between one and several, consistent with the ability of $AIM2^{PYD}$ to form filaments when expressed alone (Figure S1B).In the presence of ASC^{PYD}, $AIM2^{PYD}$ preferentially associated with ASC^{PYD} to generate short heterogeneous $AIM2^{PYD}$ filaments in complex with much longer ASC^{PYD} filaments. In contrast, Ni-NTA-gold labeling of His-tagged ASC^{PYD} in the biotinylated $AIM2^{PYD}$/ ASC^{PYD} complex showed uniform distribution along the filaments (Figure S1C), confirming that ASC^{PYD} forms the main filament body.

$AIM2^{PYD}$ and the Full-length AIM2/dsDNA Complex Nucleate ASC^{PYD} Filaments

End labeling of $AIM2^{PYD}$ suggested its role as the nucleator for directional polymerization of ASC^{PYD}.To quantitatively assess ASC^{PYD} filament formation, we set up a fluorescence polarization (FP) assay *in vitro* using a His-MBP-ASC^{PYD} fusion construct with an added C-terminal Cys for conjugating with Alexa488 fluorophore. The large fusion tag MBP inhibited ASC^{PYD} polymerization to enable His-MBP-ASC^{PYD} to be expressed in the monomeric form (Figure S1D). Polymerization of Alexa488-labeled monomeric ASC^{PYD} was initiated by addition of the TEV protease to remove His-MBP from the fusion protein. The increase in FP, which indicates ASC^{PYD} polymerization, was monitored as a function of time (Figure 1E). Although ASC^{PYD} did polymerize on its own upon His-MBP removal, the rates of polymerization were dramatically enhanced in the presence of increasing amounts of sub-stoichiometric $AIM2^{PYD}$ (1/16 – 1/2 molar ratios)(Figure 1E). The initial drop in FP corresponded with His-MBP removal by TEV and the decrease in size of ASC^{PYD}. At 5 min after TEV addition, about 75% His-MBP was removed from the fusion protein (Figure S1E). The $AIM2^{PYD}$/ASC^{PYD} filaments generated from the polymerization assay (Figure S1F) showed similar morphology to the co-expressed complex (Figure 1B).

Full-length AIM2 ($AIM2^{FL}$) is a cytosolic dsDNA sensor in which the interaction of its C-terminal HIN domain with dsDNA induces ASC recruitment and inflammasome formation. The PYD in AIM2 has been shown to interact with its HIN domain to provide auto inhibition in the absence of dsDNA binding (Jin et al., 2013). To reconstitute AIM2 inflammasome activation *in vitro*, we expressed $AIM2^{FL}$ as a His-MBP fusion. Purified His-MBP-$AIM2^{FL}$ was first incubated with equimolar 300-bp dsDNA (molar ratio calculated based on 10-bp footprint of AIM2 on dsDNA), followed by mixing withAlexa488-labeled His-MBP-ASC^{PYD}.TEV was added to remove His-MBP to initiate ASC^{PYD} polymerization as monitored by FP (Figure 1F).A dramatic increase in FP was observed upon activation of $AIM2^{FL}$ by dsDNA, recapitulating the cellular event of inflammasome activation. These data suggest that overcome of auto inhibition and oligomerization of AIM2 by dsDNA sare crucial for inducing ASC^{PYD} polymerization.

$NLRP3^{PYD\text{-}NBD}$ Nucleates and End-labels ASC^{PYD} Filaments

NLRs share similar domain architecture sand are recognized to be auto inhibited in the absence of suitable ligands. In NLRC4, an NLR with a CARD, its LRR domain plays an important role in inhibiting NLR oligomerization (Hu et al., 2013). Due to their domain similarity to Apaf-1-like molecules that form ring-like platforms through the NBDs to

induce caspase activation and apoptosis (Yuan and Akey, 2013),the overarching paradigm appears to presume that NLRP inflammasomes are also ring-like structures organized by the NBD. Formation of filamentous structures in the $AIM2^{PYD}/ASC^{PYD}$ interaction prompted us to examine ASC-dependent NLRP inflammasomes using the prototypical member NLRP3.

We expressed and purified $NLRP3^{PYD}$, $NLRP3^{PYD\text{-}NBD}$ and $NLRP3^{FL}$. While $AIM2^{PYD}$ exists as filamentous oligomers and was sufficient in promoting ASC^{PYD} polymerization, $NLRP3^{PYD}$ is a monomer and did not cause significant enhancement in ASC^{PYD} polymerization (Figure 2A). Both insect cell and *E. coli* expressed $NLRP3^{PYD\text{-}NBD}$ with inclusion of the NB Deluted from the void position of a Superdex 200 gel filtration column, and induced greatly increased ASC^{PYD} polymerization (Figure 2B). In comparison, $NLRP3^{PYD\text{-}NBD}$ is a much stronger promoter of ASC^{PYD} polymerization than $AIM2^{PYD}$; it caused significant enhancement of ASC^{PYD} polymerization at a low 1:1,600 molar ratio (Figure 2B).Notably, under the physiological intracellular condition of 140 mM KCl and 10 mM NaCl at pH 7.4 and a lower ASC concentration, ASC^{PYD} did not significantly polymerize unless increasing amounts of $NLRP3^{PYD\text{-}NBD}$ were added (Figure S2A), suggesting that ASC does not polymerize under steady physiological state without stimulation. The PYD of NLRP3 is required for ASC^{PYD} polymerization because $NLRP3^{PYD\text{-}NBD}$ proteins with mutations on PYD are compromised in this function (see below), suggesting that NBD-oligomerized $NLRP3^{PYD}$ forms the platform for ASC^{PYD} polymerization.

Insect cell expressed $NLRP3^{FL}$ showed a wide distribution on a Superdex 200 gel filtration column (Figure S2B). In keeping with auto inhibition in $NLRP3^{FL}$ as in NLRC4 (Hu et al., 2013),we found that even the highly aggregated $NLRP3^{FL}$ showed less activity than $NLRP3^{PYD\text{-}NBD}$ in promoting ASC^{PYD} polymerization because more molar quantities of $NLRP3^{FL}$ were required to achieve similar degrees of FP enhancement (Figure 2B, 2C). Despite being activated by an extensive list of stimuli, it is uncertain what constitutes the direct activator of NLRP3 (Rathinam et al., 2012). We found that addition of ATP enhanced the less aggregated fractions of recombinant $NLRP3^{FL}$ in activating ASC^{PYD} polymerization (Figure 2D); however this activation is minimal in comparison. It is likely that ATP binding by the NBD is associated with, but not sufficient for, NLRP3 activation.

Induction of ASC^{PYD} polymerization by NLRP3 suggests that NLRP3 may reside at the end of ASC^{PYD} filaments. We generated a His-MBP-$NLRP3^{PYD\text{-}NBD}$ construct capable of enzymatic biotinylation during expression. We mixed purified His-MBP-$NLRP3^{PYD\text{-}NBD}$-Biotin with His-MBP-ASC^{PYD} and added the TEV protease to cleave off His-MBP to allow ASC^{PYD} polymerization. The purified NLRP3-Biotin/ASC complex was subjected to negative stain EM and 6 nm streptavidin-gold labeling, which confirmed localization of NLRP3 to the end of ASC^{PYD} filaments (Figure 2E).Using negative stain EM, we showed that purified $NLRP3^{PYD\text{-}NBD}$ is heterogeneous with a mixture of disk-like structures and filaments (Figure S2C). The latter may represent the spiral, lock washer-like mode of oligomerization of the NBD.

Cryo-Electron Microscopy Structure of ASC^{PYD} at Near Atomic Resolution

To generate a homogeneous population of ASC^{PYD} filaments without the AIM2 or NLRP3 nucleators, we used *in vitro* ASC^{PYD} polymerization starting from purified monomeric His-MBP-ASC^{PYD} (Figure S1D). Upon TEV treatment to cleave off His-MBP, ASC^{PYD} filaments spontaneously formed as shown by cryo-EM (Figure 3A). Cryo-EM images were collected using automated data acquisition on a Titan Krios with a back thinned CMOS direct electron detector. Averaged power spectra of segments from cryo-EM images of the helical filaments showed a strong meridional reflection at 1/13.9 $Å^{-1}$, which corresponds to the reciprocal of the axial rise, but exhibited variable twist (Figure 3B, 3C), like many other helical polymers (Egelman et al., 1982). The magnitude of this variation can be seen in movie S1.

Images were processed using the Iterative Helical Real Space Reconstruction (IHRSR) method with a solid cylinder as the initial reference (Egelman, 2000). The helical heterogeneity was dealt with by sorting images by twist to generate a subset with similar helical parameters, resulting in a map at ~6Å resolution. Correction of out of plane tilt was applied to further improve the map to a conservatively estimated resolution of ~3.8 Å as determined by both Fourier shell correlation (FSC) (Rosenthal and Henderson, 2003) (Figure S3A), and comparison with the final atomic model (Figure S3B, S3C).

Rigid body fitting of the NMR structure of ASC^{PYD} (Liepinsh et al., 2003) into the cryo-EM map generated a pseudo atomic model of the ASC^{PYD} filament. The fit of the NMR structure resolved the enantiomorphic ambiguity in EM reconstructions, but even without the NMR structure the hand of the α-helices in the reconstruction was clear eliminating such ambiguities. The rigid-body fit was followed by real-space refinement (Schröder et al., 2007) to generate a final atomic model with clearly defined side chain densities (Figure 3D, 3E, S3D). The ASC^{PYD} filament is hollow with inner and outer diameters of ~20 Å and ~90 Å, respectively (Figure 4A). The polar filament has a C3 point group symmetry with 53° right-handed rotation and 14.0 Å axial rise per subunit, after correcting for a mean out-of-plane tilt of ~6°.

The structure of ASC^{PYD} in the filament exhibits conformational differences with that of ASC^{PYD} alone (Figure 4B). This is apparent in the highly variable α2-α3 loop and the short α3 helix, with clear cryo-EM density (Figure S4A). PYDs share a unique feature: the α3 helix is shortened or missing, and follows the long and flexible α2-α3 loop (Figure S4B). The conformational changes are likely due to participation of this region in all three types of interactions in the filament (see below and Figure S3D). Although the ASC^{PYD} alone structure was determined at a pH below 4.0 (Liepinsh et al., 2003), lack of significant conformational differences else where and absence of acidic residues in α3 helix support the structural changes as due to filament formation. Among known PYD structures, $NLRP3^{PYD}$ and $ASC2^{PYD}$ possess a conformation similar to the filament conformation of ASC^{PYD} (Figure 4C), suggesting that $NLRP3^{PYD}$ and $ASC2^{PYD}$ may be better interactors with ASC^{PYD}.The former similarity may account for the high efficiency of $NLRP3^{PYD\text{-}NBD}$ in promoting ASC^{PYD} polymerization (Figure 2B).ASC2 is a PYD only protein that is highly homologous to ASC^{PYD} and has been shown to associate with ASC to modulate caspase-1

activation (Stehlik et al., 2003).If ASC2 can be incorporated into ASC^{PYD} filaments but lacks the effect or CARD, it could inhibit caspase-1 recruitment and activation. One face of a cross section of the filament is largely negatively charged while the opposite face is largely positively charged (Figure 4D), suggesting the role of charge complementarity in filament assembly.

Detailed Interactions in the ASC^{PYD} Filament

There are three major asymmetric interfaces (types I, II, III) in the filament, one within each of the three-start helical strands (type I), and two between the strands (type II and III) (Figure 4E). Remarkably, despite being within the DD superfamily, the PYD/PYD interactions show remarkable differences to the DD complex structures (Figure 4F and S4C–E, Table S1). If one of the subunits is aligned, the corresponding partner subunit would need to rotate by 15–26°, 21–35° and 18–52° for the type I, II and III interfaces respectively, relative to the corresponding interfaces in the MyD88/IRAK4/IRAK2 DD complex and the PIDD/RAIDD DD complex (Ferrao and Wu, 2012; Lin et al., 2010; Park et al., 2007) (Figure S4C–E, Table S1). Relatively, the structural superposition indicates that the type I interaction is the most conserved, which is also the most dominant, burying about 880 $Å^2$ of surface area. Type II and III interactions are highly variable and bury 540 $Å^2$ and 360 $Å^2$ of surface area, respectively. Structural differences between PYD and other members of the DD fold superfamily, and formation of a substantial central cavity may have shifted the relative orientations of the subunits in the type I, II and III interactions.

In the previously observed DD/DD interactions, type I is mediated by residues at α1 and α4 (type Ia) and residues at α2 and α3 (type Ib) (Ferrao and Wu, 2012; Lin et al., 2010; Park et al., 2007). Despite being the most conserved, the relative shift in orientation and the structural differences between DDs and PYDs minimized the involvement of α3 in the intra-strand type I PYD/PYD interaction (Figure 4G, S3D). In the inter-strand type II PYD/PYD interaction, residues at the α4-α5corner of one ASC^{PYD} (type IIa) and residues at the α5-α6 corner of the second ASC^{PYD} (type IIb) mediate this interaction (Figure 4H, Fig. S3D). In the inter-strand type III PYD/PYD interaction, α2-α3 corner of one ASC^{PYD} (type IIIa) interacts with the α1-α2 corner (type IIIb) of the other subunit (Figure 4I,S3D). Prominently, the PYD-unique and highly variable α2-α3 loop participates in all three types of PYD/PYD interactions (Figure S3D), which may explain the conformational changes in this region upon filament formation (Figure 4B). Overall the interactions contain charged, hydrophilic and hydrophobic components, with charge interactions playing an important role (Figure S4F–H). Consistently, ASC^{PYD} polymerization exhibits salt dependence (Figure S4I).

Structure-based Mutagenesis *in Vitro* and in Cells

Structure-guided mutagenesis *in vitro* confirmed the role of type I, II and III interactions in ASC^{PYD} filament formation, as shown by elution in more monomeric fractions (Figure 5A). In particular, K21Q, K21E/K22E, K26E, R41E, D48R, D48N and D51R of the type I interface, F59E of the type II interface, and E13R and R41E of the type III interface, abolished filament formation (Figure 5A, Table S2). Additional mutations, R3E and L50A of the type I interface, and Y36A and E80R of the type II interface, weakened filament

formation as shown by increased presence in the monomeric fractions in comparison with the wild type (WT) (Figure 5A, Table S2). Mutations that disrupted filament formation *in vitro* also abrogated the ability of eGFP-ASC^{PYD} to form filaments in cells as shown by confocal and fluorescence microscopy (Figure 5B, S5A–B) and by EM of immuno purified samples (Figure S5C–D). A previous extensive mutagenesis study on surface exposed charged residues confirmed the importance of additional observed interfacial residues in ASC^{PYD} filament formation in cells (Moriya et al., 2005) (Table S2).

In contrast to disruptive phenotypes of mutations on interfacial residues, the charge reversal mutation E67Routside the interface did not affect eGFP-ASC^{PYD} filament formation (Figure 5C). At the type I interface, K21, D48 and D51 interact with each other (Figure 4G) and mutations on each of the residues disrupt filament formation (Figure 5A, 5B). Remarkably, the triple charge reversal mutant K21E/D48K/D51K rescued eGFP-ASC^{PYD} filament formation in cells (Figure 5C), supporting the validity of the structurally observed interactions.

Modeled AIM2^{PYD}/ASC^{PYD} and NLRP3$^{PYD\text{-}NBD}$/ASC^{PYD} Interactions

The ASC^{PYD} filament structure provides a template for modeling the AIM2^{PYD}/ASC^{PYD} and NLRP3^{PYD}/ASC^{PYD} hetero-PYD/PYD interactions using the published crystal structures of AIM2^{PYD} (Jin et al., 2013) and NLRP3^{PYD} (Bae and Park, 2011). End locations of AIM2^{PYD} and NLRP3^{PYD} in their complexes with ASC^{PYD} filaments suggest that the PYDs in AIM2 and NLRP3 continue the helical arrangement seen in the ASC^{PYD} filament using a combination of the same type I, II and III interactions (Figure 5D). Given the observed conformational changes at the α2-α3 corner, which points down in the helical diagram (Figure 4D), we reasoned that AIM2 and NLRP3 PYDs should reside above the ASC^{PYD} filament (Figure 5D).

We selected residues in AIM2^{PYD} and NLRP3^{PYD} structures corresponding to those in ASC^{PYD} that caused impairment in filament formation when mutated (Figure 5A, 5B). Assaying the ability of AIM2^{PYD} and NLRP3$^{PYD\text{-}NBD}$ mutants in promoting ASC^{PYD} polymerization showed that mutations on each of the predicted interfaces in AIM2^{PYD}, including L10A/L11A, R24E and F27G of the type I interface, Y74R of the type II interface, and G38E, K39E and D15R of the type III interface, either abolished or showed greatly reduced promotion of ASC^{PYD} polymerization (Figure 5E, Table S3). Additionally, in a recently published study on AIM2^{PYD}, the D19A/E20A/E21A/D23A mutation, which harbors mostly type I interface residues, abolished the interaction with ASC^{PYD} (Jin et al., 2013). Similarly, mutations at each of the predicted type I, II and III interfacial residues on NLRP3^{PYD}, including K23E/K24E and M27E of the type I interface, E64R and D82R of the type II interface, and R43W and E15R of the type III interface, caused almost complete impairment in promoting ASC^{PYD} polymerization by the NLRP3$^{PYD\text{-}NBD}$ construct (Figure 5F, Table S3). It should be noted because AIM2^{PYD} also aggregates into similar filaments (Figure S1B), the same mutations would likely affect both AIM2/ASC interaction and AIM2 self-association. For NLRP3, the PYD does not self-associate while the NBD mediates self-association; therefore the PYD mutations in NLRP3 would directly affect ASC interaction. Collectively, these data support that the interactions in the ASC^{PYD} filament also define the

mode of hetero-oligomerization in the AIM2^{PYD}/ASC^{PYD} and NLRP3^{PYD}/ASC^{PYD} interaction pairs.

Reconstitution of the TernaryAIM2 Inflammasome

The C-termini of ASC^{PYD} subunits extend prominently outward from the filament (Figure6A), providing a connection to the CARD in ASC after a 23-residue linker. Superposition of the NMR structure of ASC^{FL} (de Alba, 2009) with ASC^{PYD} in the filament displayed the flexibly linked, peripheral ASC^{CARD} (Figure 6B). To reveal the structural architecture of full ternary inflammasomes, we expressed and purified His-GFP-caspase-1^{CARD}, His-MBP-ASC^{FL} and His-MBP-AIM2^{PYD}. We mixed the three proteins with the TEV protease to allow His-MBP removal and formation of a ternary complex. His-tag pull down showed that His-GFP-caspase-1^{CARD} interacted with ASC^{FL} and AIM2^{PYD} (Figure 6C). The stoichiometry between ASC^{FL} and AIM2^{PYD} in the ternary complex is consistent with that in the AIM2^{PYD}/ASC^{PYD} binary complex with AIM2^{PYD} under-stoichiometric (Figure 1C). ASC in turn appeared under-stoichiometric tocaspase-1. EM showed that the ternary complex is star-shaped (Figure 6D). Anti-ASC immuno gold-labeling (15 nm) showed that ASC resides in the center of the stars (Figure 6D). In contrast, Ni-NTA conjugated with 6 nm gold particles labeled His-GFP-caspase-1^{CARD} along the arms of the stars (Figure 6E). These data suggest that AIM2^{PYD} nucleates short filaments of ASC^{FL} through PYD/PYD interactions and ASC^{CARD} further initiates caspase-1^{CARD} filaments to promote caspase-1 activation. Because the linker between ASC PYD and CARD is flexible, the outer CARDs should be able to cluster together and act as the platform for caspase-1 polymerization (Figure 6B).

We tested the role of ASC^{CARD} in inflammasome assembly using a caspase-1^{CARD} polymerization assay. We used “sandwich”-tagged His-MBP-caspase-1^{CARD}-Sumo construct because N-terminally tagged His-MBP-caspase-1^{CARD} construct still formed filaments. Asortase motif was added for fluorophore labeling (Theile et al., 2013). Polymerization of caspase-1^{CARD} was initiated by addition of TEV to cleave off His-MBP and monitored by fluorescence polarization. In the presence ASC^{FL} or ASC^{CARD} at sub-stoichiometric ratios, caspase-1^{CARD} polymerization was greatly enhanced (Figure 6F), consistent with nucleation of caspase-1 polymerization by ASC.

It is intriguing that the ASC^{FL} component in the ternary complex does not display as long filaments as in the binary AIM2^{PYD}/ASC^{PYD} or NLRP3$^{PYD\text{-}NBD}$/ASC^{PYD} complexes. We reasoned that since His-MBP-ASC^{FL} forms bundled clusters minutes after removal of the His-MBP tag (Figure S6A) and precipitates, likely due to the CARD and its potential to crosslink filaments, ASC^{FL} might only exist as short filaments such that almost all ASC^{CARD} molecules are in complex with caspase-1^{CARD}. To determine if the same ASC^{PYD} interactions in the observed filament govern those in the context of ASC^{FL}, we co-transfected Myc-His-tagged ASC^{FL} with WT and mutant ASC^{PYD}-eGFP in 293T cells. Immuno precipitated with anti-His antibody followed by anti-eGFP Western showed that Myc-His-ASC^{FL} pulled down WT ASC^{PYD}-eGFP, but was severely impaired in interacting with ASC^{PYD}-eGFP that harbors mutations on residues important for the ASC^{PYD} filament formation (Figure 6G, S6B). We further tested the effects of PYD mutations in ASC^{FL} using

the *in vitro* inflammasome reconstitution assay. His-GFP-caspase-1^{CARD} pulled down $AIM2^{PYD}$ in the presence of WT ASC^{FL}, but not mutant ASC^{FL} defective in formation of PYD filaments (Figure S6C), demonstrating that the same interactions in the PYD filaments govern the interaction in the ternary inflammasome complex.

Morphology and Stoichiometry of Endogenous NLRP3 Inflammasome

Our data suggest a unified model of inflammasome assembly in which AIM2 upon dsDNA interaction or NLRP3 upon activation nucleates ASC helical clusters through PYD/PYD interactions (Figure 6H). The oligomerized ASC CARDs then form the platform for caspase-1^{CARD} to nucleate into filaments, which in turn bring caspase domains into proximity for dimerization, transauto-cleavage and activation (Figure 6H). To elucidate the morphology of endogenous inflammasomes, we stimulated THP-1 cells with uric acid crystals, immuno precipitated the activated NLRP3 inflammasome using anti-ASC antibody, and subjected the immuno precipitated sample to negative stain EM. The images contained both single filaments (Figure 7A) and intertwined filaments (FS7A); the former resemble sub complexes of *in vitro* reconstituted inflammasomes and the latter resemble clustered, ball of yarn-like reconstituted inflammasomes that form upon overnight incubation (FS7B).

It has been shown previously that upon stimulation, each cell forms one gigantic NLRP3 punctum adjacent to the nucleus (Fernandes-Alnemri et al., 2007). To visualize the structure of such a punctum *in situ*, we expressed ASC-eGFP in COS-1 cells and performed immuno gold EM on ultra thin cryo sections that preserve native structures. Control cells transfected with eGFP alone showed neither punctum nor anti-ASC gold labeling, and ASC-eGFP transfected cells did not exhibit gold labeling in the absence of the anti-ASC primary antibody (Figure S7C).Specific gold labeling was shown in ASC-eGFP transfected cells in the presence of anti-ASC primary antibody and protein A-gold (10 nm) treatment (Figure 7B). The labeling revealed a densely packed perinuclear punctum of about 2 μm in size, in contrast to the hollow structure implicated previously (Masumoto et al., 1999). The dense structures are consistent with the ball of yarn-like architectures of *in vitro* reconstituted and in cell immuno precipitated inflammasomes.

In vitro reconstitution of the ternary inflammasome suggests an over-stoichiometry of caspase-1 to ASC (Figure 6C). To determine if endogenous ASC-dependent inflammasomes from cells also possess the similar property, we stimulated THP-1 cells with uric acid crystals, immuno precipitated the activated NLRP3 inflammasome using anti-ASC antibody, and performed quantitative Western blotting using recombinant caspase-1 and ASC as standards. These experiments showed that caspase-1 is over-stoichiometric to ASC, by ~3.5-fold in the current experiment (Figure 7C, 7D, S7D, S7E). It should be noted that an anti-ASC antibody would have precipitated both ASC alone and its complex with caspase-1 and therefore the measured 3.5- fold over-stoichiometry should be an under estimation.

Structure-guided PYD Mutations Compromise IL-1β Processing

One main biological consequence of inflammasome activation is the processing of prolL-1β by caspase-1 to IL-1β. To address the consequence of structure-based mutations in biological function, we used a co-transfection strategy to assay IL-1β processing (Jin et al.,

2012). Co-transfect ion of caspase-1, proIL-1β and ASC did not cause significant cleavage of proIL-1β into mature IL-1β (Figure 7E). While addition of WT AIM2 activated the inflammasome and led to IL-1β production, co-transfection of PYD-interaction defective AIM2 mutants compromised IL-1β conversion (Figure 7E), demonstrating the functional consequence of observed PYD/PYD interactions.

DISCUSSION

A Near Atomic Resolution Structure by Cryo-EM

Our reconstruction of a small, structurally variable biological sample represents a significant advance in high-resolution structure determination by cryo-EM made possible by automated microscopy (Potter et al., 1999), a state-of-the-art electron microscope (the Titan Krios), and a new generation of direct electron detectors (Bai et al., 2013; Bammes et al., 2012; Li et al., 2013; Liao et al., 2013), combined with existing computational approaches for variable twist polymers (Egelman, 2000; Egelman et al., 1982). Most of the structures that have been currently solved by cryo-EM to near-atomic resolution are icosahedral viruses that are highly ordered and with a high degree of internal symmetry (Zhou, 2011). In the absence of any mechanism to maintain long-range order all biological polymers will display cumulative disorder (Egelman and DeRosier, 1982). We think that the new hardware and software advances in cryo-EM will have an enormous impact in allowing many biological polymers, including those whose helical symmetry could not even be determined with confidence, to now be reconstructed at near-atomic resolution.

PYD/PYD Interactions

The ASC^{PYD} filament structure presented here provides insights into molecular mechanisms of homo- and hetero-PYD associations in inflammasomes. Among the PYDs with known structures, NLRP3,NLRP 12, AIM2 and ASC2 have been shown to interact with ASC (Rathinam et al., 2012; Stehlik et al., 2003). Consistently, they exhibit the highest sequence conservation at the ASC-interaction surfaces with 61%, 54%, 50%, and 89% homology, respectively (Table S4). The ASC^{PYD} structure may also provide a template for other PYDs with no structures such as the $IFI16^{PYD}$ filament cooperatively assembled on dsDNA (Morrone et al., 2013).

A number of mutations in NLRP3, NLRP12 and MEFV have been shown to associate with hereditary periodic fever syndromes. For NLRP3, all mutations are dominant and likely cause activation by overcoming auto inhibition (Touitou et al., 2004). For NLRP12, a nonsense mutation and a splicing defect generate truncated proteins at residues 284 and 646, respectively, and cause spontaneous inflammation (Jeru et al., 2008), suggesting that the PYD and part of the NBD are sufficient for inflammasome formation and activation. For MEFV, hundreds of variants, most of which are associated with Familial Mediterranean Fever (FMF), have been identified (Touitou et al., 2004). Gene insertion “knockin” (KI) mouse models with three frequent FMF-associated mutations (M680I, M694V, and V726A) showed that they caused severe spontaneous inflammatory phenotypes (Chae et al., 2011). Most relevant to the PYD interactions, six mutants, T12I, Y19C, K25R, R39G, E84K and A89T, have been mapped to the PYD of MEFV (Touitou et al., 2004). None of these

residues directly map to the PYD/PYD interaction surfaces (Figure S3D), and may therefore act by overcoming auto inhibition.

A Unified Assembly Mechanism for Inflammasomes

Our data here present a mechanism for the assembly of ASC-dependent inflammasomes, in which AIM2 and NLRP3 both nucleate helical ASC clusters through PYD/PYD interactions, and ASC in turn nucleates caspase-1 filaments through CARD/CARD interactions (Figure 6H). These minimal structures coalesce to form the micron-sized, dense structures we observed *in situ*.We propose that CARD-containing NLRs (NLRCs), which are independent of ASC, may also form filamentous structures by directly promoting caspase-1 polymerization through CARD/CARD interactions. Therefore, the mechanism of nucleation-induced filament formation may extend beyond ASC-dependent inflammasomes. It has been shown that uncleavedcaspase-1 catalytic domain forms dimers in crystals (Elliott et al., 2009); the dimerization may occur within caspase-1 filaments in inflammasomes, resulting in intradimer cleavage, stabilization of dimerization, and enhancement of enzymatic activity.

Recent studies have revealed that in many innate immune pathways, multiple intracellular signaling proteins assemble into higher-order signaling machines for transmission of receptor activation information to cellular responses, with implicated new molecular mechanisms for threshold behavior, time delay of activation, and temporal and spatial control of signal transduction (Wu, 2013). Here we show that inflammasomes also assemble into higher-order signal osomes that likely impart similar properties to its activation and kinetics. In this scenario, upon reaching the NLRP3 or AIM2 activation threshold, caspase-1 may polymerize until its concentrations falls below the dissociation constant. Given that caspase-1is over-stoichiometric to ASC by just a few fold, the average lengths of individual ASC nucleated caspase-1 filaments in cells may be shorter than those reconstituted *in vitro*, leading to punctate, rather than filamentous morphology of intact inflammasomes. Once formed, inflammasomes may require active processes such as autophagy for their degradation (Saitoh et al., 2008).This scenario is reminiscent of the case for the filamentous CARMA1/Bcl10/MALT1 signal osome (Qiao et al., 2013), and may represent a general mechanism of disassembly of higher-order signalosomes in innate immunity to terminate signaling.

EXPERIMENTAL PROCEDURES

Recombinant Protein Expression and Purification

Various His-, His-MBP- and His-MBP-Sumo “sandwich”-tag fusion constructs or co-expression constructs of AIM2, ASC, caspase-1 and NLRP3 were expressed in *E. coli* and insect cells. Biotinylation was performed in *E. coil* by co-expression with biotin ligase. All mutations in this construct were introduced using the QuikChange mutagenesis protocol.

Polymerization Assays

His-MBP-ASC^{PYD} and His-MBP-caspase-1^{CARD}-Sumo were labeled with Alexa488 and TAMRA fluorophores, respectively. Filament formation was monitored using fluorescence

polarization upon addition of TEV protease to remove His-MBP, in the presence and absence of various nucleators of polymerization.

Nanogold and Immunogold EM

Standard protocols were used for streptavidin-gold labeling of biotinylated proteins, Ni-NTA-nanogold labeling of His-tagged proteins, and immunogold labeling by appropriate antibodies using negative stain EM. ASC-transfected COS-1 cells were pelleted, fixed, flash frozen and ultra thin sectioned for immuno gold EM and contrasting with uranylacetete.

Cryo-EM, Image Processing and Refinement

Grids containing ASC^{PYD} were imaged using an FEI Titan Krios electron microscope operating at 300 keV, and recorded using a 4k × 4k Falcon II direct electron detector with a back thinned CMOS chip. The images were processed with SPIDER (Frank et al., 1996) and the IHRSR algorithm (Egelman, 2000) was used for helical reconstruction. The ASC^{PYD} NMR structure (PDB ID 1UCP) (Liepinsh et al., 2003) was chosen as the starting model and the refinement was carried out using DireX (Schröder et al., 2007). We estimate the resolution of the reconstruction at ~3.8 Åas determined by both Fourier shell correlation and comparison with the final atomic model.

AIM2 Inflammasome Reconstitution

HEK293T cells were transfected with pEFBOS-C-term-Guassia luciferase/Flag pro-IL-1β (~54 kDa), pro-caspase-1, HA-ASC, and the full-length wild type or mutant Flag-AIM2 expression constructs using Gene Juice (Novagen). Cell lysates were probed with mouse anti-IL1β monoclonal antibody. Expression of ASC and AIM2 was detected using anti-Flag and anti-HA antibodies, respectively.

Supplementary Material

Refer to Web version on PubMed Central for supplementary material.

Acknowledgments

We thank NatachaOpalka, Seth Darst, Leona Cohen-Gould, Maria Ericsson, William Rice and MarienaSilvestry Ramos for help with EM imaging, Harry Leung for help with confocal microscopy, Gabriel Nuñez for providing cDNAs, and the National Institutes of Health for funding supports (EB001567 to E.H.E and AI083713 to K.A.F.).

REFERENCES

Bae JY, Park HH. Crystal structure of NALP3 protein pyrin domain (PYD) and its implications in inflammasome assembly. J Biol Chem. 2011; 286:39528–39536. [PubMed: 21880711]

Bai XC, Fernandez IS, McMullan G, Scheres SH. Ribosome structures to near-atomic resolution from thirty thousand cryo-EM particles. Elife. 2013; 2:e00461. [PubMed: 23427024]

Bammes BE, Rochat RH, Jakana J, Chen DH, Chiu W. Direct electron detection yields cryo-EM reconstructions at resolutions beyond 3/4 Nyquist frequency. J Struct Biol. 2012; 177:589–601. [PubMed: 22285189]

Chae JJ, Cho YH, Lee GS, Cheng J, Liu PP, Feigenbaum L, Katz SI, Kastner DL. Gain-of-function Pyrin mutations induce NLRP3 protein-independent interleukin-1beta activation and severe autoinflammation in mice. Immunity. 2011; 34:755–768. [PubMed: 21600797]

de Alba E. Structure and interdomain dynamics of apoptosis-associated speck-like protein containing a CARD (ASC). J Biol Chem. 2009; 284:32932–32941. [PubMed: 19759015]

Egelman EH. A robust algorithm for the reconstruction of helical filaments using single-particle methods. Ultramicroscopy. 2000; 85:225–234. [PubMed: 11125866]

Egelman EH, DeRosier DJ. The Fourier transform of actin and other helical systems with cumulative random angular disorder. Acta Cryst. 1982; A38:796–799.

Egelman EH, Francis N, DeRosier DJ. F-actin is a helix with a random variable twist. Nature. 1982; 298:131–135. [PubMed: 7201078]

Elliott JM, Rouge L, Wiesmann C, Scheer JM. Crystal structure of procaspase-1 zymogen domain reveals insight into inflammatory caspase autoactivation. J Biol Chem. 2009; 284:6546–6553. [PubMed: 19117953]

Fernandes-Alnemri T, Wu J, Yu JW, Datta P, Miller B, Jankowski W, Rosenberg S, Zhang J, Alnemri ES. The pyroptosome: a supramolecular assembly of ASC dimers mediating inflammatory cell death via caspase-1 activation. Cell Death Differ. 2007; 14:1590–1604. [PubMed: 17599095]

Ferrao R, Wu H. Helical assembly in the death domain (DD) superfamily. Curr Opin Struct Biol. 2012; 22:241–247. [PubMed: 22429337]

Franchi L, Munoz-Planillo R, Nunez G. Sensing and reacting to microbes through the inflammasomes. Nat Immunol. 2012; 13:325–332. [PubMed: 22430785]

Frank J, Radermacher M, Penczek P, Zhu J, Li Y, Ladjadj M, Leith A. SPIDER and WEB: processing and visualization of images in 3D electron microscopy and related fields. J Struct Biol. 1996; 116:190–199. [PubMed: 8742743]

Hu Z, Yan C, Liu P, Huang Z, Ma R, Zhang C, Wang R, Zhang Y, Martinon F, Miao D, et al. Crystal structure of NLRC4 reveals its autoinhibition mechanism. Science. 2013; 341:172–175. [PubMed: 23765277]

Jeru I, Duquesnoy P, Fernandes-Alnemri T, Cochet E, Yu JW, Lackmy-Port-Lis M, Grimprel E, Landman-Parker J, Hentgen V, Marlin S, et al. Mutations in NALP12 cause hereditary periodic fever syndromes. Proc Natl Acad Sci U S A. 2008; 105:1614–1619. [PubMed: 18230725]

Jin T, Perry A, Jiang J, Smith P, Curry JA, Unterholzner L, Jiang Z, Horvath G, Rathinam VA, Johnstone RW, et al. Structures of the HIN domain:DNA complexes reveal ligand binding and activation mechanisms of the AIM2 inflammasome and IFI16 receptor. Immunity. 2012; 36:561–571. [PubMed: 22483801]

Jin T, Perry A, Smith PT, Jiang J, Xiao TS. Structure of the AIM2 pyrin domain provides insights into the mechanisms of AIM2 autoinhibition and inflammasome assembly. J Biol Chem. 2013

Lamkanfi M, Dixit VM. Inflammasomes and their roles in health and disease. Annu Rev Cell Dev Biol. 2012; 28:137–161. [PubMed: 22974247]

Li X, Mooney P, Zheng S, Booth CR, Braunfeld MB, Gubbens S, Agard DA, Cheng Y. Electron counting and beam-induced motion correction enable near-atomic-resolution single-particle cryo-EM. Nat Methods. 2013; 10:584–590. [PubMed: 23644547]

Liao M, Cao E, Julius D, Cheng Y. Structure of the TRPV1 ion channel determined by electron cryo-microscopy. Nature. 2013; 504:107–112. [PubMed: 24305160]

Liepinsh E, Barbals R, Dahl E, Sharipo A, Staub E, Otting G. The death-domain fold of the ASC PYRIN domain, presenting a basis for PYRIN/PYRIN recognition. J Mol Biol. 2003; 332:1155–1163. [PubMed: 14499617]

Masumoto J, Taniguchi S, Ayukawa K, Sarvotham H, Kishino T, Niikawa N, Hidaka E, Katsuyama T, Higuchi T, Sagara J. ASC, a novel 22-kDa protein, aggregates during apoptosis of human promyelocytic leukemia HL-60 cells. J Biol Chem. 1999; 274:33835–33838. [PubMed: 10567338]

Masumoto J, Taniguchi S, Sagara J. Pyrin N-terminal homology domain-and caspase recruitment domain-dependent oligomerization of ASC. Biochem Biophys Res Commun. 2001; 280:652–655. [PubMed: 11162571]

Medzhitov R, Janeway C Jr. Innate immune recognition: mechanisms and pathways. Immunol Rev. 2000; 173:89–97. [PubMed: 10719670]

Moriya M, Taniguchi S, Wu P, Liepinsh E, Otting G, Sagara J. Role of charged and hydrophobic residues in the oligomerization of the PYRIN domain of ASC. Biochemistry. 2005; 44:575–583. [PubMed: 15641782]

Morrone SR, Wang T, Constantoulakis LM, Hooy RM, Delannoy MJ, Sohn J. Cooperative assembly of IFI16 filaments on dsDNA provides insights into host defense strategy. Proc Natl Acad Sci U S A. 2013

Potter CS, Chu H, Frey B, Green C, Kisseberth N, Madden TJ, Miller KL, Nahrstedt K, Pulokas J, Reilein A, et al. Leginon: a system for fully automated acquisition of 1000 electron micrographs a day. Ultramicroscopy. 1999; 77:153–161. [PubMed: 10406132]

Qiao Q, Yang C, Zheng C, Fontan L, David L, Yu X, Bracken C, Rosen M, Melnick A, Egelman EH, et al. Structural Architecture of the CARMA1/Bcl10/MALT1 Signalosome: Nucleation-Induced Filamentous Assembly. Mol Cell. 2013; 51:766–779. [PubMed: 24074955]

Rathinam VA, Vanaja SK, Fitzgerald KA. Regulation of inflammasome signaling. Nat Immunol. 2012; 13:333–332. [PubMed: 22430786]

Rosenthal PB, Henderson R. Optimal determination of particle orientation, absolute hand, and contrast loss in single-particle electron cryomicroscopy. J Mol Biol. 2003; 333:721–745. [PubMed: 14568533]

Saitoh T, Fujita N, Jang MH, Uematsu S, Yang BG, Satoh T, Omori H, Noda T, Yamamoto N, Komatsu M, et al. Loss of the autophagy protein Atg16L1 enhances endotoxin-induced IL-1beta production. Nature. 2008; 456:264–268. [PubMed: 18849965]

Schröder GF, Brunger AT, Levitt M. Combining efficient conformational sampling with a deformable elastic network model facilitates structure refinement at low resolution. Structure. 2007; 15:1630–1641. [PubMed: 18073112]

Stehlik C, Krajewska M, Welsh K, Krajewski S, Godzik A, Reed JC. The PAAD/PYRIN-only protein POP1/ASC2 is a modulator of ASC-mediated nuclear-factor-kappa B and pro-caspase-1 regulation. Biochem J. 2003; 373:101–113. [PubMed: 12656673]

Strowig T, Henao-Mejia J, Elinav E, Flavell R. Inflammasomes in health and disease. Nature. 2012; 481:278–286. [PubMed: 22258606]

Theile CS, Witte MD, Blom AE, Kundrat L, Ploegh HL, Guimaraes CP. Site-specific N-terminal labeling of proteins using sortase-mediated reactions. Nat Protoc. 2013; 8:1800–1807. [PubMed: 23989674]

Touitou I, Lesage S, McDermott M, Cuisset L, Hoffman H, Dode C, Shoham N, Aganna E, Hugot JP, Wise C, et al. Infevers: an evolving mutation database for auto-inflammatory syndromes. Hum Mutat. 2004; 24:194–198. [PubMed: 15300846]

Wu H. Higher-order assemblies in a new paradigm of signal transduction. Cell. 2013; 153:287–292. [PubMed: 23582320]

Yin Q, Sester DP, Tian Y, Hsiao YS, Lu A, Cridland JA, Sagulenko V, Thygesen SJ, Choubey D, Hornung V, et al. Molecular mechanism for p202-mediated specific inhibition of AIM2 inflammasome activation. Cell Rep. 2013; 4:327–339. [PubMed: 23850291]

Yuan S, Akey CW. Apoptosome structure, assembly, and procaspase activation. Structure. 2013; 21:501–515. [PubMed: 23561633]

Zhou ZH. Atomic resolution cryo electron microscopy of macromolecular complexes. Adv Protein Chem Struct Biol. 2011; 82:1–35. [PubMed: 21501817]

- AIM2 and NLRP3 inflammasomes are filamentous assemblies *in vitro* and in cells
- 3.8 Å Cryo-EM structure of ASC^{PYD} depicts the underlying oligomerization mechanism
- Fluorescence polarization assays suggest nucleation-induced filament formation
- ASC-dependent inflammasomes use a polymerization mechanism for caspase-1 activation

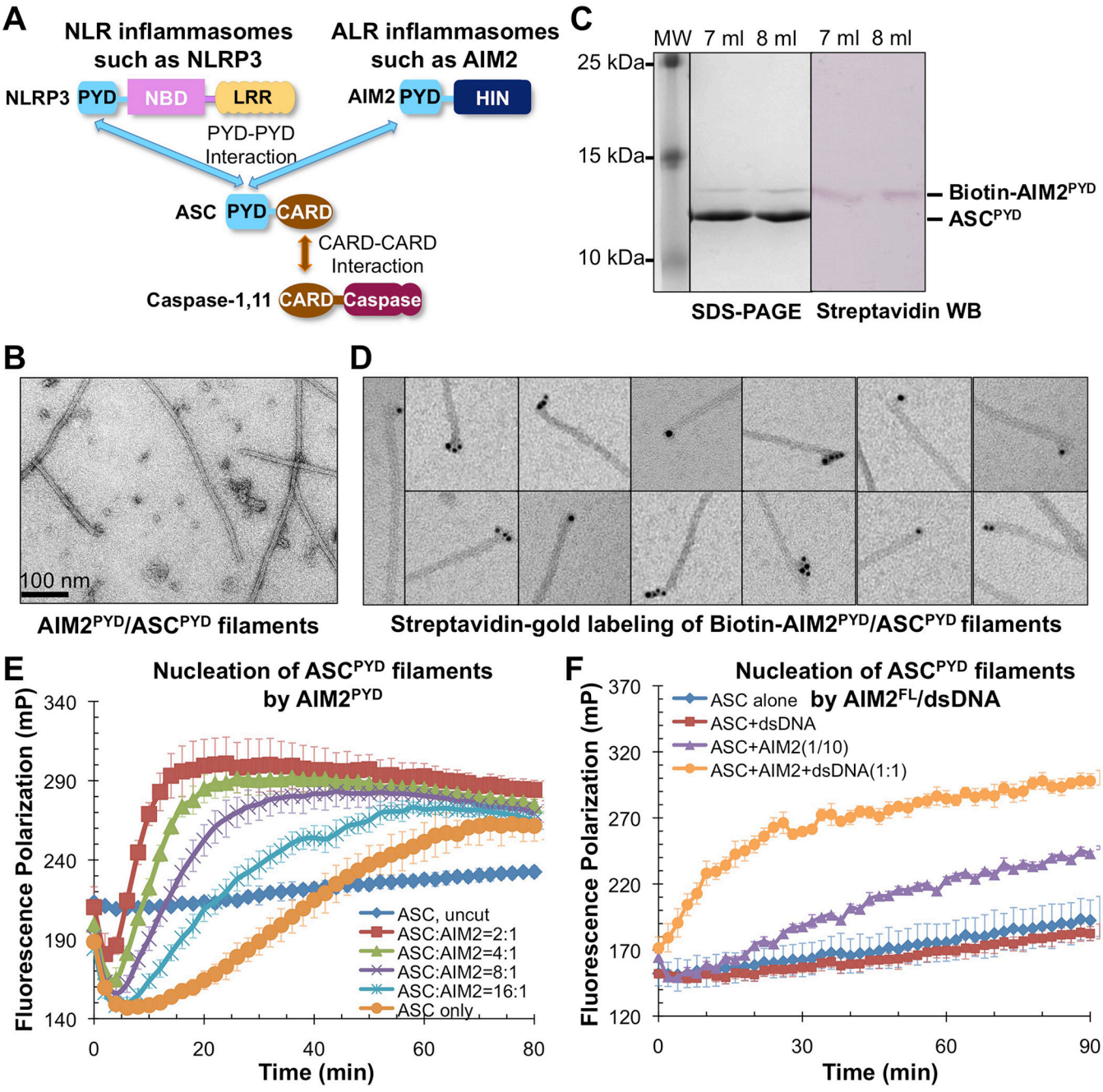

Figure 1. AIM2 Promotes Formation of ASC^{PYD} Filaments

A. Domain composition and interaction hierarchy of NLRP3 and AIM2 inflammasomes.

B. An electron micrograph of the AIM2^{PYD}/ASC^{PYD} binary complex.

C. Gel filtration fractions of biotinylated AIM2^{PYD}/ASC^{PYD} complex as visualized by Coomassie Blue-stained SDS-PAGE (left) and streptavidin-alkaline phosphatase Western blot (right). **D**. Labeling of biotinylated AIM2^{PYD}/ASC^{PYD} binary complex by streptavidin-gold conjugate (6nm).

E. Fluorescence polarization (FP) assay of AIM2^{PYD}-nucleated ASC^{PYD} filament formation. mP: unit for FP. Data are represented as mean±SD (N=3).

F. Effect of dsDNA on AIM2^{FL}-nucleated ASC^{PYD} filament formation. 2 μM of AIM2^{FL} monomer from gel filtration was incubated with or without equimolar300-bp dsDNA (assuming a 10-bp footprint of AIM2 for molar calculation) for 30 minutes before diluting to a working concentration 0.1 μM (ASC^{PYD}:AIM2^{FL}=10:1) for the FP assay. Data are represented as mean±SD (N=3).

See also Figure S1.

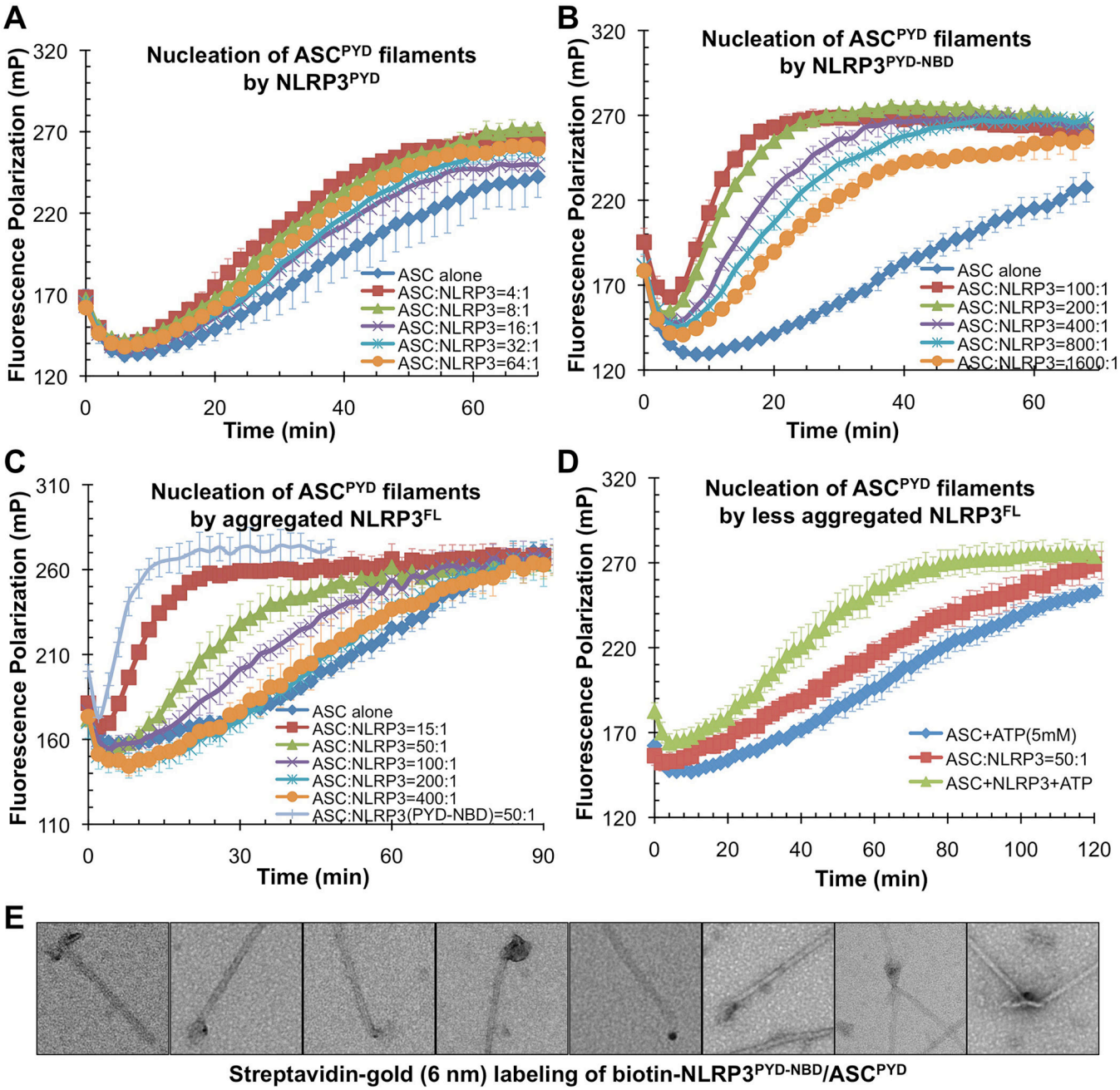

Figure 2. NLPR3^{FL} and NLRP3$^{PYD-NBD}$ but not NLRP3^{PYD} Promote ASC^{PYD} Filament Formation

A, B, C.Nucleation of ASC^{PYD} filaments by titrating increasing amounts of NLRP3^{PYD} (A), NLRP3$^{PYD-NBD}$ (B), NLRP3^{FL} (C) as monitored by fluorescence polarization. Data are represented as mean±SD (N=3).

D. A less aggregated gel filtration fraction of NLRP3 was subjected to ASC^{PYD} polymerization assay with or without 5mM ATP. Data are represented as mean±SD (N=3).

E. Streptavidin-gold (6nm) labeling of biotinylated NLRP3$^{PYD-NBD}$/ASC^{PYD} binary complex.

See also Figure S2.

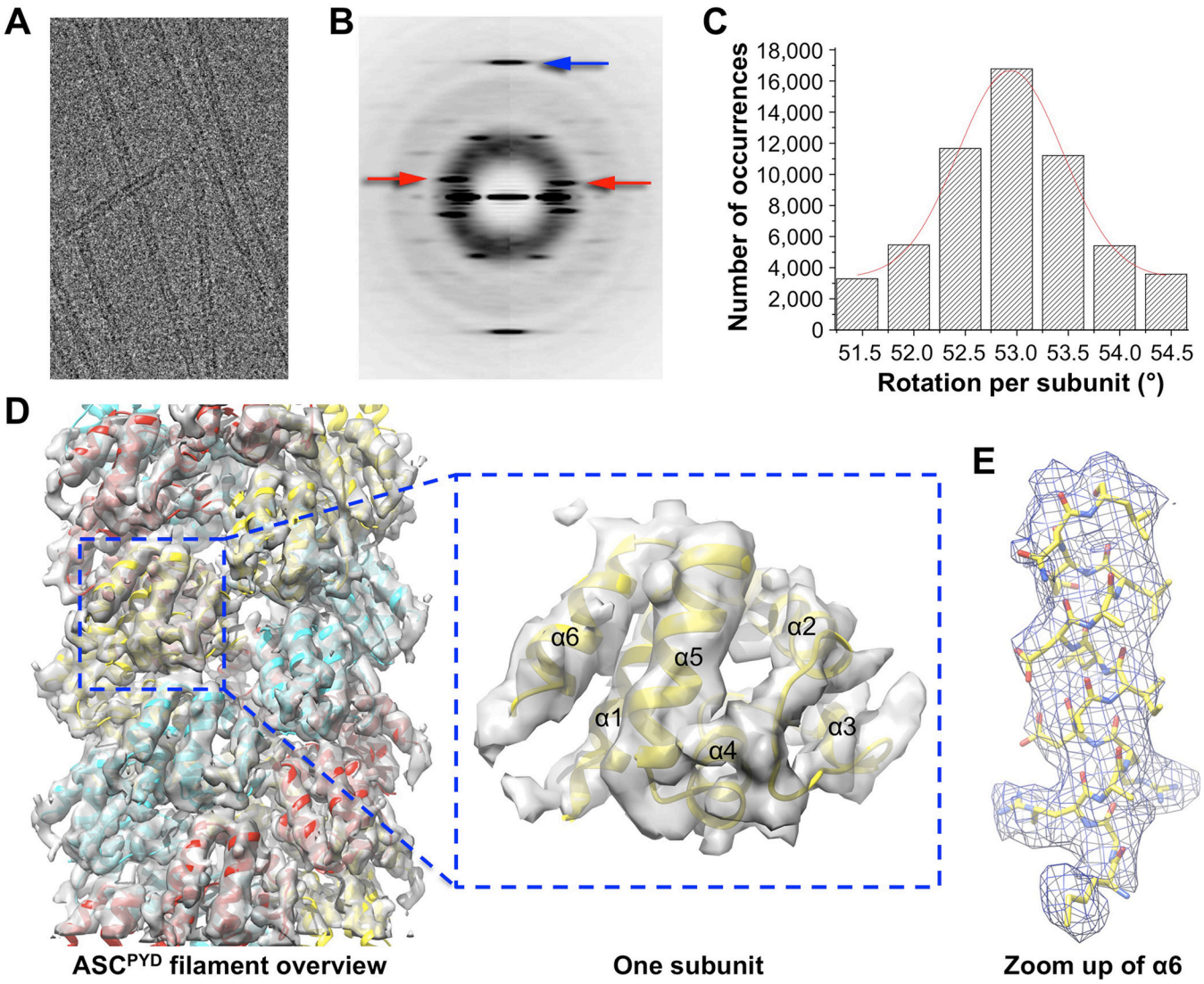

Figure 3. Cryo-EM Structure of the ASC^{PYD} Filament at Near Atomic Resolution

A. A cryo-EM image of ASC^{PYD} filaments.

B. Average power spectra of ASC^{PYD} filaments in two twist bins (left and right halves) showing constant axial rise per subunit (blue arrow) and variable long-range twist features (red arrows).

C. Filament segments can be divided into separate twist bins according to azimuth angle, or rotation per subunit.

D. Cryo-EM reconstruction of the ASC^{PYD} filament, superimposed with the final atomic model shown in three colors each for one start of the three-start helical assembly.

E. A zoom up view of helix α6 shown in stick model and superimposed with the EM density.

See also Figure S3 and Movie S1.

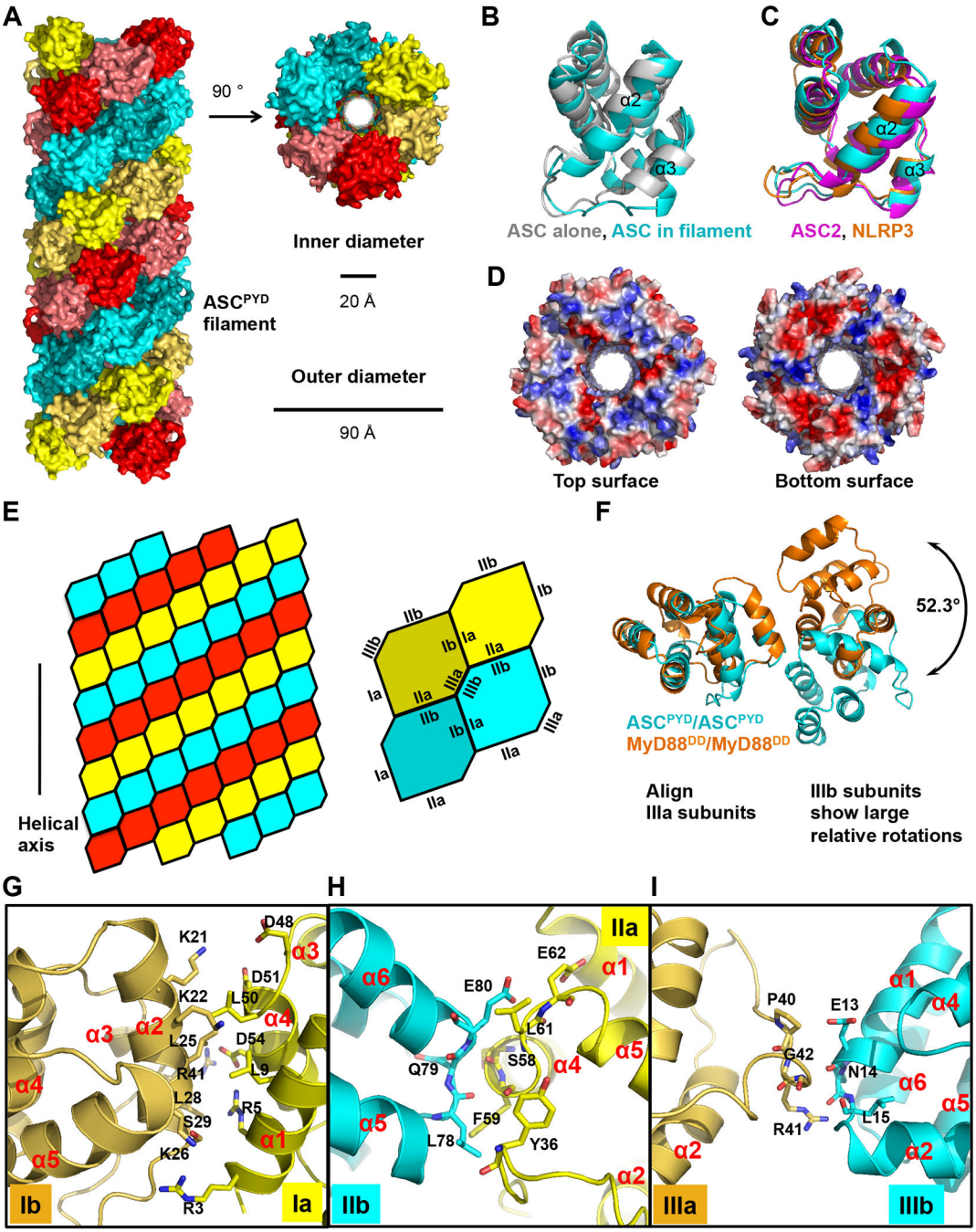

Figure 4. Detailed Cryo-EM Model of the ASC^{PYD} Filament

A. The ASC^{PYD} filament is a three-start helical assembly with C3 symmetry as shown in a surface representation. The three-start helical strands are denoted by red, cyan, and yellow, respectively, with alternating darker and lighter shades to show subunit boundaries.

B. Comparison of the initial ASC^{PYD} subunit model (gray, PDB: 1UCP) and the subunit structure after refinement against the cryo-EM density (cyan).

C.Structures of ASC2^{PYD} (magenta) and NLRP3^{PYD} (orange) are similar to the ASC^{PYD} subunit structure in the filament (cyan).

D.Electrostatic surface representations of approximate cross sections of the filament.

E. A schematic diagram of the ASC^{PYD} filament and the three types of asymmetric interactions, defined in accordance with the previously observed DD/DD interactions.

F. Comparison of the Type III interactions in the ASC^{PYD} filament (cyan) and in the MyD88/IRAK4/IRAK2 DD complex (orange).

G, H, I. Detailed interactions in Type I, II, and III interfaces, respectively. Side chains of interfacial residues are shown as stick models and labeled.

See also Figure S4.

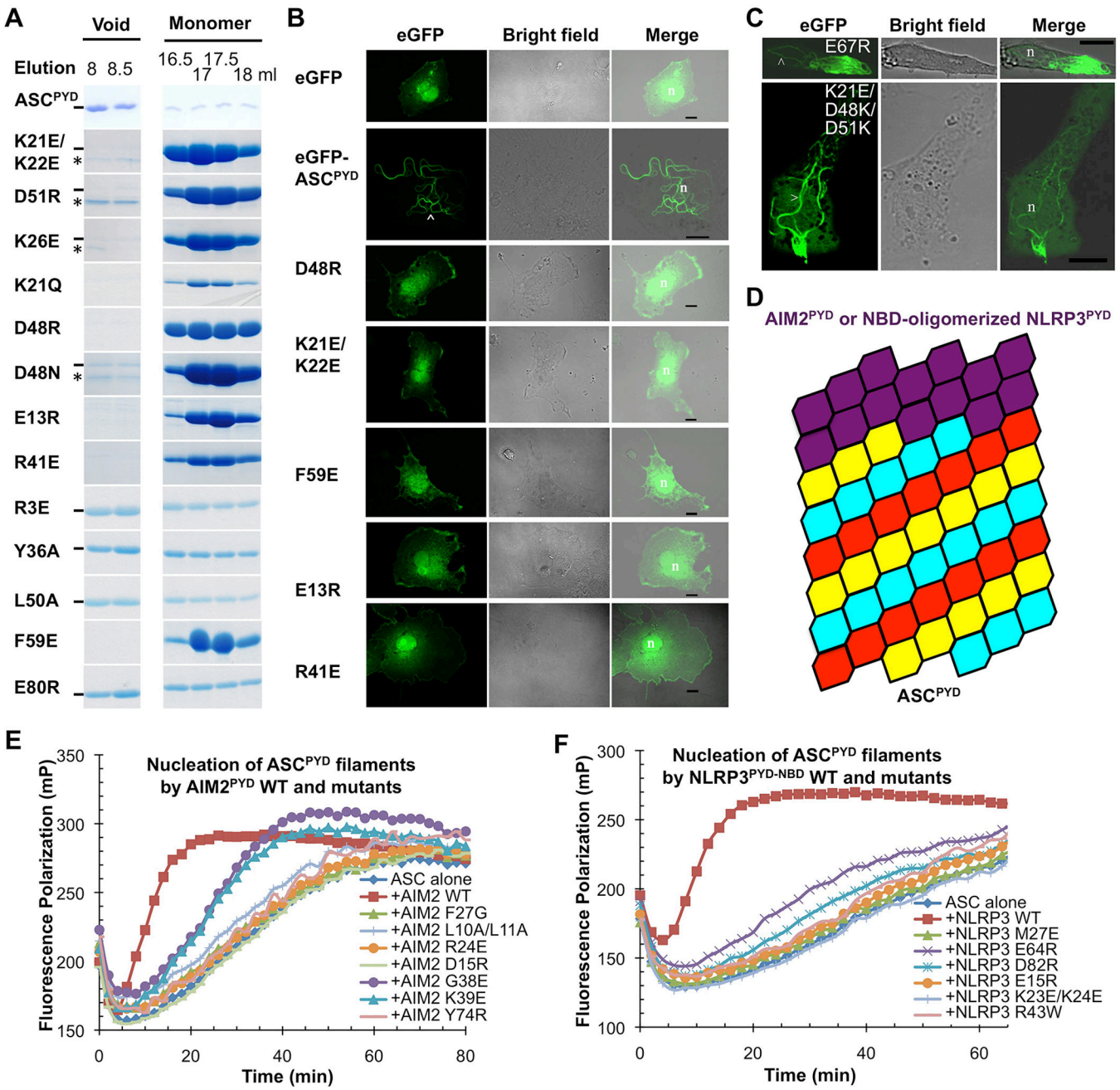

Figure 5. Structure-based Mutations Disrupts ASC^{PYD} Filament Formation, AIM2^{PYD}/ASC^{PYD} Interaction and NLRP3^{PYD}/ ASC^{PYD} Interaction *in Vitro* and in Cells

A. Size-exclusion chromatography of WT and mutant ASC^{PYD} showing both filamentous (void) and monomeric fractions from a Superdex 200 column. Hyphen denotes ASC^{PYD} and asterisk denotes a contaminant.

B. Morphology of transfected WT and mutant eGFP-tagged ASC^{PYD} constructs visualized by confocal laser scanning microscopy. The arrowhead depicts filaments. n: nucleus; scale bars = 10μm.

C.Morphology of transfected eGFP-tagged ASC^{PYD} visualized by confocal laser scanning microscopy. Top: ASC^{PYD} with charge reversal mutation on a residue outside the filament interface. Bottom: ASC^{PYD} with triple charge reversal mutation that rescued the defectiveness of the single mutants. Arrow heads depict filaments.

D.A schematic model of AIM2^{PYD}/ASC^{PYD} or NLRP3^{PYD}/ASC^{PYD} filaments composed of a top AIM2^{PYD} or NLRP3^{PYD} layer extended by ASC^{PYD} filament body.

E,F. Mutations of conserved interfacial residues on AIM2^{PYD} (E) and NLRP3$^{PYD-NBD}$ (F) reduced or abolished their ability to nucleate ASC^{PYD} filaments.

See also Figure S5.

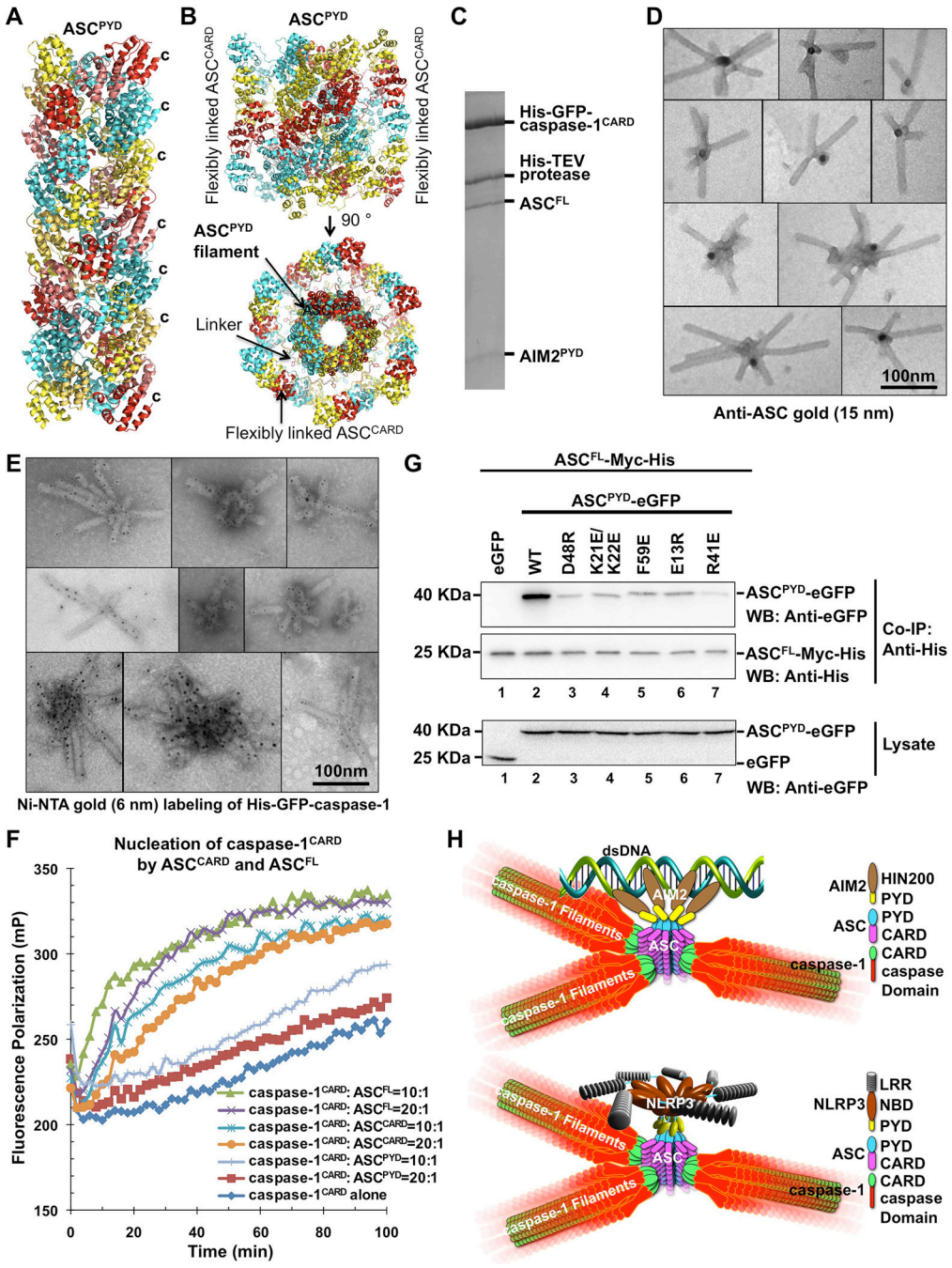

Figure 6. Reconstitution of the Full Ternary AIM2 Inflammasome

A. The ASC^{PYD} filament structure in a ribbon representation. The protruding C-termini for connecting to ASC^{CARD} are labeled for the subunits at the right.

B. ASC^{FL} NMR structure (PDB: 2KN6) is superimposed on the ASC^{PYD} model to show the outward located ASC^{CARD}.

C. Pull-down of the core AIM2 inflammasome *in vitro* as visualized on Coomassie-Blue stained SDS-PAGE.

D, E.Electron micrographs of His-GFP-caspase-1^{CARD}/ASC^{FL}/AIM2^{PYD} ternary complex labeled with anti-ASC gold (**D**) and Ni-NTA gold (**E**).

F. Promotion ofHis-MBP-caspase-1^{CARD}-Sumo (3 μM) polymerization by ASC^{FL} or ASC^{CARD} at sub stoichiometric ratios of 1:20 and 1:10 upon removal of His-MBP by TEV. ASC^{PYD} did not enhance caspase-1^{CARD} polymerization.

G. Mutations in ASC^{PYD} reduced its binding to ASC^{FL}. ASC^{FL}-Myc-His was co-transfected with WT and mutant ASC^{PYD}-eGFP. Immuno precipitation and Western blotting was carried out using anti-His and anti-eGFP antibodies respectively.

H. Model of inflammasome assembly. Up stream sensing proteins such as AIM2 and NLRP3 oligomerize upon activation to form a platform of PYDs that induces ASC filament assembly through PYD/PYD interactions. Multiple ASC^{CARD} molecules cluster to promotecaspase-1 filament formation through CARD/CARD interactions. Proximity induced dimerization of the caspase domain activates the enzyme followed by auto-cleavage.

See also Figure S6.

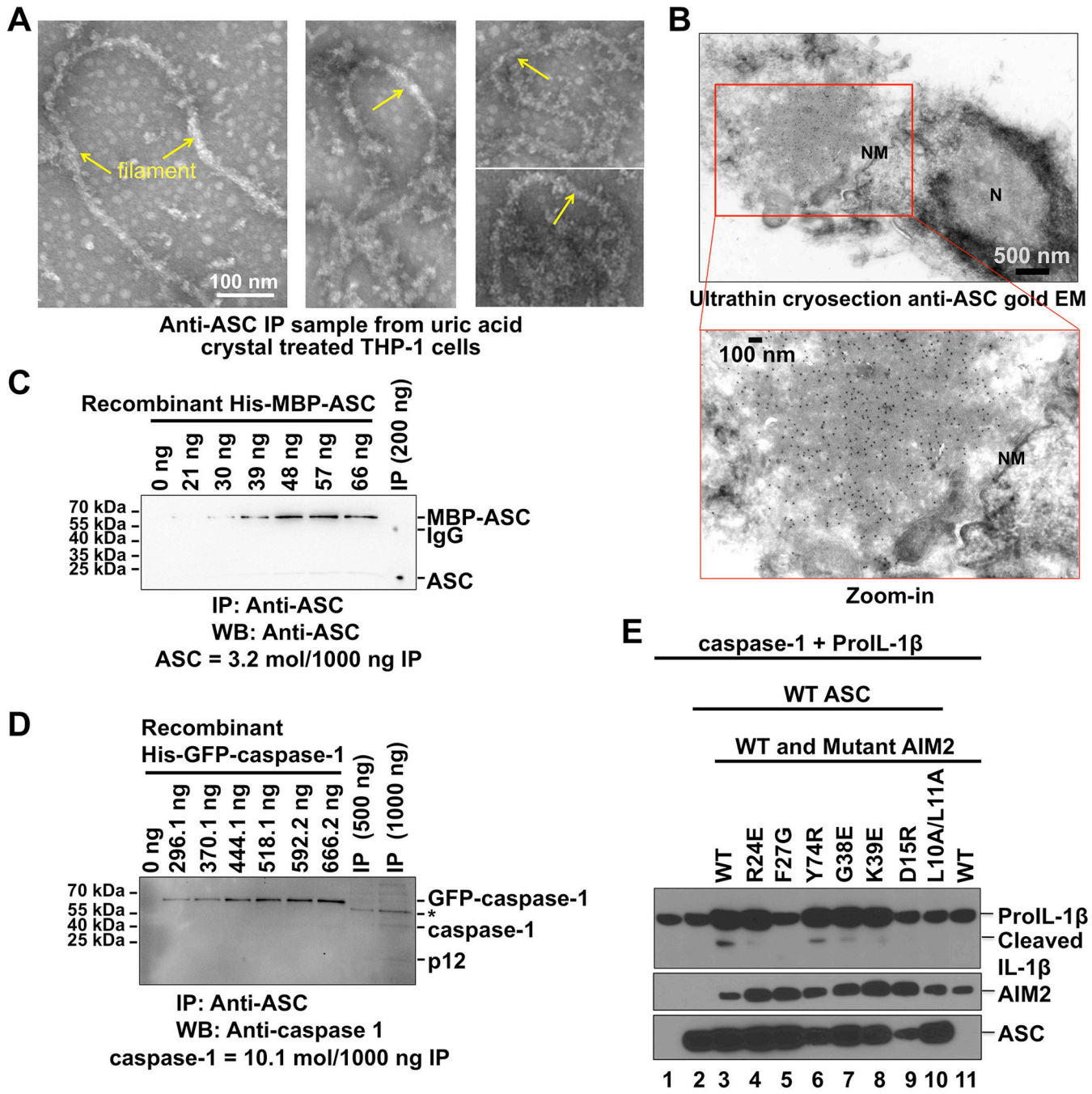

Figure 7. Morphology, Stoichiometry and ProIL-1β Processing in Inflammasomes

A. Morphology of anti-ASC immuno precipitated NLRP3 inflammasomes from uric acid crystal activated THP-1 cells analyzed by negative stain EM. Arrows denote filaments.

B. Immuno gold EM on ultra thin cryo sections from ASC^{FL}-eGFP transfected COS-1 cells. The ASC-containing compact structure is densely decorated by gold particles (10 nm). N, nucleus; NM, nuclear membrane.

C, D. Quantification of immuno precipitated ASC-containing complex (IP) from uric acid crystal activated THP-1 cells using quantitative anti-ASC (C)and anti-caspase-1 p12 (D) Western blotting. Known amounts of recombinant His-MBP-ASC and His-

GFP-caspase-1 were Western blotted to generate standard curves. The full-length caspase-1 and the cleaved p12 bands were both included in the quantification.

E. AIM2 inflammasome reconstitution in HEK293T cells to define the functional consequence of structure-based mutations in AIM2. Cells were co-transfected with plasmids encoding proIL-1β and caspase-1 (lane 1), plus ASC alone (lane 2), or WT AIM2 alone (lane 11), or ASC together with WT or indicated AIM2 mutants (lanes 3 to 10). Maturation of proIL-1βinto biologically active IL-1β was detected by Western blotting using anti-IL-1β antibody (top panel).The expression levels of HA-ASC and Flag-AIM2 were detected by Western blotting using anti-HA and anti-Flag antibodies (lower panels).

See also Figure S7.